Anomalous magneto-optical response of black phosphorus thin films

Xiaoying Zhou,[1] Wen-Kai Lou,[1] Feng Zhai,[2] and Kai Chang[1,*]

[1]*SKLSM, Institute of Semiconductors, Chinese Academy of Sciences, Post Office Box 912, Beijing 100083, China*

[2]*Department of Physics, Zhejiang Normal University, Jinhua 321004, China*

(Received 28 July 2015; revised manuscript received 23 September 2015; published 7 October 2015)

We theoretically investigate the Landau levels (LLs) and magneto-optical conductivity (MOC) of black phosphorus thin films under a perpendicular magnetic field based on an effective $\boldsymbol{k}\cdot\boldsymbol{p}$ Hamiltonian and linear-response theory. We obtain the analytical expression for LLs, which agrees well with the numerical calculations, and find that the LLs sublinearly depend on the magnetic field and LL index. By using the Kubo formula, we evaluate the longitudinal and Hall optical conductivities as functions of the photon energy and the magnetic field. The analytical optical transition matrix elements reveal unusual selection rules for the interband (intraband) optical transitions between the LLs $\Delta n = 0, \pm 2$ ($\pm 1, \pm 3$). The MOC shows strongly anisotropic behaviors of the band structure. For the interband transition, the MOC for linearly polarized light along the armchair direction is three orders of magnitude larger than that along the zigzag direction. Interestingly, we find a beating pattern in the interband MOC due to the interference among the three kinds of optical transitions. For the intraband transition, the MOC can be used to determine the band parameters such as the effective masses and the interband coupling at zero magnetic field. Our results about the MOC can also be applied to the monolayer black phosphorus.

DOI: 10.1103/PhysRevB.92.165405 PACS number(s): 78.20.Ls, 42.70.−a, 81.05.Zx

I. INTRODUCTION

The group-V element phosphorus has several allotropes and black phosphorus (BP) is the most stable phase under normal conditions [1]. Recently, layered BP has attracted intensive attention because of its unique electronic properties and potential applications in nanoelectronics [2–6]. Bulk BP is a van der Waals bonded layered material where each layer forms a puckered surface due to sp^3 hybridization [2,3]. BP possesses a direct band gap of 0.3 eV located at the Z point [3,4]. This direct gap moves to the Γ point and increases to 1.5–2 eV when the thickness decreases from bulk to few layers and eventually monolayer via mechanical exfoliation [3,5,7]. Hence, BP is an appealing candidate for tunable photodetection from the visible to the infrared part of the electromagnetic spectrum [8]. Further, the field effect transistor based on few layer BP is found to have an on/off ratio of 10^5 and a carrier mobility at room temperature as high as 10^3 cm^2/V s [3,5], which make BP a favorable material for the next generation of electronics.

The low-energy dispersion of bulk BP around the Z point can be well described by an anisotropic two-band $\boldsymbol{k}\cdot\boldsymbol{p}$ Hamiltonian [9]. One can obtain the low-energy Hamiltonian for BP thin films (TFs) by applying a confinement in the perpendicular z direction. To date, various interesting properties for BP TFs have been predicted theoretically and verified experimentally, including those related to the strain induced gap modification [2], tunable optical properties [10], layer controlled anisotropic excitons [11], anisotropic Landau levels (LLs) [12], quantum oscillations [13,14], and quantum Hall effect [15]. However, less attention has been paid to the magneto-optical properties of BP TFs [16–18]. Magneto-optics is one of the most accurate investigations of the band structure of metals and semiconductors in experiments, which has been applied successfully in graphene [19].

*To whom correspondence should be addressed: kchang@semi.ac.cn

In this work, we theoretically investigate the LLs and magneto-optical conductivity (MOC) of BP TFs subjected to a vertical magnetic field. Based on an effective $\boldsymbol{k}\cdot\boldsymbol{p}$ Hamiltonian, we obtain the analytical expression for LLs, which agrees well with the numerical calculations, and find that the LLs sublinearly depend on the magnetic field and LL index. By using the Kubo formula, we evaluate the longitudinal and Hall magneto-optical conductivities as functions of the photon energy and the magnetic field. The analytical optical transition matrix elements reveal unusual selection rules for the interband (intraband) optical transitions between LLs $\Delta n = 0$, ± 2 ($\pm 1, \pm 3$). The MOC shows strongly anisotropic behaviors of the band structure. For the interband transition, the MOC for linearly polarized light along the armchair direction is three orders of magnitude larger than that along the zigzag direction. Interestingly, we find a beating pattern in the interband MOC due to the interference among three kinds of optical transitions. For the intraband transition, the MOC can be used to determine the band parameters such as the effective masses and the interband coupling at zero magnetic field.

The paper is organized as follows. In Sec. II, we present the calculation of LLs numerically and analytically. In Sec. III, we calculate the magneto-optical transition matrix elements. In Sec. IV, we calculate the longitudinal and Hall magneto-optical conductivity and present the numerical results and discussions. Finally, we summarize our results in Sec. V.

II. LANDAU LEVELS OF BP THIN FILMS

The low-energy dispersion of bulk BP can be well described by a two band effective $\boldsymbol{k}\cdot\boldsymbol{p}$ Hamiltonian, which is given by [9,16]

$$H=\begin{pmatrix} E_c+\alpha_c k_x^2+\beta_c k_y^2+\eta_c k_z^2 & \gamma k_x \\ \gamma k_x & E_v-\alpha_v k_x^2-\beta_v k_y^2-\eta_v k_z^2 \end{pmatrix}, \quad (1)$$

where $E_c = 0.15$ eV ($E_v = -0.15$ eV) is the conduction-band (valence-band) edge; $\alpha_{c,v}$, $\beta_{c,v}$, and $\eta_{c,v}$ are related to the

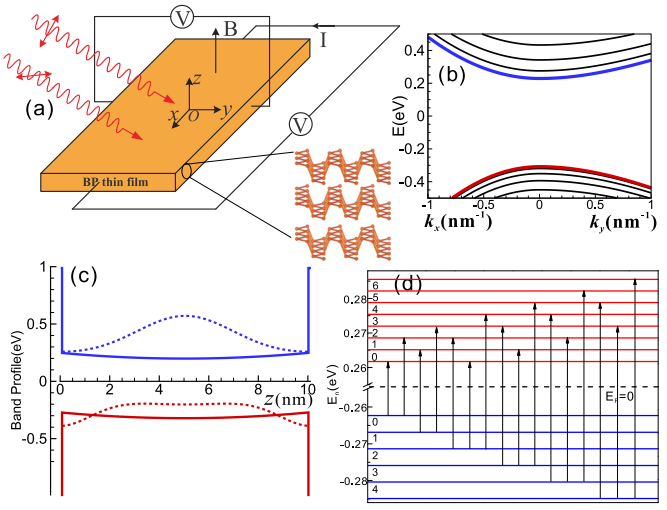

FIG. 1. (Color online) (a) Schematic illustration of magneto-optical setup on BP TF structure. The wavy lines represent linearly polarized light. The lattice structure of the BP TF is shown on the right. (b) Band structure for 10-nm BP thin film obtained from self-consistent calculations. (c) The probability distribution and band profile for the lowest sub-band along the z direction for 10-nm BP TFs obtained from self-consistent calculation. The carrier density (hole doped) used in the self-consistent calculation is 3.0×10^{12} cm^{-2}. (d) Schematic illustration of the dominated interband transitions. The interband transitions mainly occur when LL index changes $\Delta n = 0, \pm 2$ [Eq. (18)].

effective masses by $\alpha_{(c,v)} = \hbar^2/2m_{(c,v)x}$, $\beta_{(c,v)} = \hbar^2/2m_{(c,v)y}$, and $\eta_{(c,v)} = \hbar^2/2m_{(c,v)z}$, with [9] $m_{cx} = 0.151\ m_e$, $m_{cy} = 1.062\, m_e, m_{cz} = 0.292\, m_e, m_{vx} = 0.122\, m_e, m_{vy} = 0.708\, m_e$, and $m_{vz} = 0.607\ m_e$; m_e is the free electron mass; and $\gamma = \hbar v_f$ describes the interband coupling between conduction and valence band with $v_f = 3.5 \times 10^5$ m/s. For BP TFs [see Fig. 1(a)], broken translation symmetry in the z direction moves the gap from the Z point in bulk to the Γ point. Assuming a hard wall boundary condition in the z direction, the Hamiltonian for the j sub-band of BP TFs with N layers is

$$H_N^j = \begin{pmatrix} E_c^j + \alpha_c k_x^2 + \beta_c k_y^2 & \gamma k_x \\ \gamma k_x & E_v^j - \alpha_v k_x^2 - \beta_v k_y^2 \end{pmatrix}, \quad (2)$$

where the band edge is modified as $E_c^j = E_g^N/2 + \eta_c k_{z,j}^2$, $E_v^j = -E_g^N/2 - \eta_v k_{z,j}^2$, $k_{z,j} = \sqrt{j^2 - 1}\pi/L_z$ is the discrete wave vector along the z direction (L_z is the thickness of the BP film), and E_g^N is the band gap of N-layer BP. In the GW approximation, the band gap is given by [11] $E_g^N = E_g^1/N^{0.73} + E_g^\infty$, where $E_g^1 = 2.0$ eV and $E_g^\infty = 0.3$ eV are the band gap of monolayer and bulk BP, respectively. Typically, for a 20 layer ($N = 20$) BP TF ($L_z \approx 10$ nm), the band gap is 0.52 eV. Obviously, this Hamiltonian is highly anisotropic. The corresponding eigenstates along the z direction are $|\varphi_j(z)\rangle (j = 1,2,3,\ldots)$ which are orthogonal with each other. This means that the optical transitions between different sub-bands are prohibited. Keeping this in mind, we will omit this factor in the rest of the context for brevity. Considering the interband coupling correction to the effective masses around the Γ point along the k_x direction, one obtains the modified effective masses [12]: $m'_{cx} = \hbar^2/2(\alpha + \gamma^2/E_g^j)$ and $m'_{vx} = \hbar^2/2(\lambda + \gamma^2/E_g^j)$. For the lowest sub-band, the modified effective masses around the Γ point along the k_x direction are $m'_{cx} = 0.108\ m_e$ and $m'_{vx} = 0.092\ m_e$. In contrast, the effective masses around the Γ point along the k_y direction remain unchanged.

When a perpendicular magnetic field $\boldsymbol{B} = (0,0,B)$ is applied, taking Landau gauge $\boldsymbol{A} = (-By,0,0)$, we define the creation and annihilation operators as

$$\hat{a} = \sqrt{\frac{m_{cy}\omega_c}{2\hbar}}\left(y - y_0 + i\frac{p_y}{m_{cy}\omega_c}\right),$$
$$\hat{a}^\dagger = \sqrt{\frac{m_{cy}\omega_c}{2\hbar}}\left(y - y_0 - i\frac{p_y}{m_{cy}\omega_c}\right), \quad (3)$$

where $\omega_c = eB/(m_{cx}m_{cy})^{\frac{1}{2}}$ is the cyclotron frequency, $y_0 = l_B^2 k_x$ is the cyclotron center, and $l_B = \sqrt{\hbar/eB}$ is the magnetic length. We find that Hamiltonian (2) becomes

$$H_N^j = H_0 + H' + H'', \quad (4)$$

with

$$H_0 = \begin{pmatrix} E_c^j + (\hat{a}^\dagger\hat{a} + 1/2)\hbar\omega_c & 0 \\ 0 & E_v^j - (\hat{a}^\dagger\hat{a} + 1/2)\hbar\omega_v \end{pmatrix},$$
$$H' = \hbar\omega_\gamma(\hat{a} + \hat{a}^\dagger)\sigma_x, \quad H'' = (\hat{a}^2 + \hat{a}^{\dagger 2})\hbar\omega' \frac{\sigma_z - 1}{2},$$

where σ_x and σ_z are Pauli matrices, $\omega_\gamma = \gamma/\sqrt{2}\hbar l_B \alpha_{yx}$, $\omega_v = (r_x + r_y)\omega_c$, $\omega' = (r_x - r_y)\omega_c/2$ with $\alpha_{yx} = (m_{cy}/m_{cx})^{\frac{1}{4}}$, and $r_i = m_{ci}/m_{vi} (i = x,y)$. H' and H'' describe the interband (intraband) couplings. We should point out that the interband coupling becomes important as the thickness of the BP TF increases. While for the monolayer BP with large band gap (about 2.0 eV) the interband coupling is weak, the decoupled Hamiltonian can give independent LLs for conduction and valence bands, respectively [12]. For thick BP TFs, the interband coupling cannot be neglected, especially for interband optical transition due to small band gap (about 0.52 eV). The eigenvalues and corresponding eigenvectors of H_0 are given by

$$E_{c,n}^{(0)} = E_c^j + (n + 1/2)\hbar\omega_c, \psi_{c,n}^{(0)} = \begin{pmatrix} |n\rangle \\ 0 \end{pmatrix},$$
$$E_{v,n}^{(0)} = E_v^j - (n + 1/2)\hbar\omega_v, \psi_{v,n}^{(0)} = \begin{pmatrix} 0 \\ |n\rangle \end{pmatrix}, \quad (5)$$

where $|n\rangle$ are the eigenvectors of number operator $\hat{n} = \hat{a}^\dagger\hat{a}$. In real-space representation, $\langle y|n\rangle = \phi_n[\kappa(y - y_0)]$ are the wave-functions of a one-dimensional harmonic oscillator with center y_0 and $\kappa = \sqrt{m_{cy}\omega_c/\hbar}$. Numerically, the eigenvalues and eigenvectors can be evaluated by taking the eigenvectors of H_0 as basis functions. In this basis, the wave function of the system can be expressed as

$$\psi(x,y) = \frac{e^{ik_x x}}{\sqrt{L_x}} \sum_{m=0}^{M} \begin{pmatrix} c_m \\ d_m \end{pmatrix} \phi_m[\kappa(y - y_0)]. \quad (6)$$

Then, we can diagonalize the Hamiltonian (4) numerically in a truncated Hilbert space and obtain the eigenvalues as well as the eigenvectors. However, in the low-energy regime, it is easy to find that $\sqrt{n}\hbar\omega_c \ll (E_{c,n}^{(0)} - E_{v,n}^{(0)})$ and

$|\omega'/\omega_v| = 0.048 \ll 1$, which means that we can treat H' and H'' as perturbations to H_0 in Eq. (4). Including the energy correction to the second order, the LLs of BP TFs are given by

$$\begin{aligned} E_{c,n} &= E_{c,n}^{(0)} + \frac{n\hbar^2\omega_\gamma^2}{E_g^j + n\hbar\omega_+ + \frac{1}{2}\hbar\omega_-} \\ &\quad + \frac{(n+1)\hbar^2\omega_\gamma^2}{E_g^j + (n+1)\hbar\omega_+ - \frac{1}{2}\hbar\omega_-}, \\ E_{v,n} &= E_{v,n}^{(0)} - \frac{n\hbar^2\omega_\gamma^2}{E_g^j + n\hbar\omega_+ - \frac{1}{2}\hbar\omega_-} \\ &\quad - \frac{(n+1)\hbar^2\omega_\gamma^2}{E_g^j + (n+1)\hbar\omega_+ + \frac{1}{2}\hbar\omega_-} - \frac{\hbar\omega'^2}{\omega_v}(2n+1), \end{aligned} \tag{7}$$

where $\omega_\pm = \omega_c \pm \omega_v$, and $E_g^j = E_c^j - E_v^j$ is the band gap of the jth sub-band. Obviously, this LL spectra sublinearly depend on the LL index and magnetic field. Further, we find the LL spacings are

$$\begin{aligned} E_{c,n+1} - E_{c,n} &\approx \hbar\omega_c + \frac{2E_g^j\hbar^2\omega_\gamma^2}{(E_g^j + n\hbar\omega_+)\left[E_g^j + (n+2)\hbar\omega_+\right]}, \\ E_{v,n} - E_{v,n+1} &\approx \hbar\omega_v' + \frac{2E_g^j\hbar^2\omega_\gamma^2}{(E_g^j + n\hbar\omega_+)\left[E_g^j + (n+2)\hbar\omega_+\right]}, \end{aligned} \tag{8}$$

where $\omega_v' = \omega_v + 2\omega'^2/\omega_v$. From Eq. (8), we find that the LL spacings decrease with increasing LL index, which will induce a redshift in the magneto-optical conductivity. Meanwhile, the corresponding wave function to the first-order correction is

$$\psi_{c,n} = a_n\psi_{c,n}^{(0)} + a_{n-1}\psi_{v,n-1}^{(0)} + a_{n+1}\psi_{v,n+1}^{(0)}, \tag{9}$$

$$\psi_{v,n} = b_n\psi_{v,n}^{(0)} + b_{n-1}\psi_{c,n-1}^{(0)} + b_{n+1}\psi_{c,n+1}^{(0)}, \tag{10}$$

where $a_n = (1 + a_{n-1}'^2 + a_{n+1}'^2)^{-\frac{1}{2}}$, $b_n = (1 + b_{n-1}'^2 + b_{n+1}'^2)^{-\frac{1}{2}}$ with

$$\begin{aligned} a_{n-1}' &= \frac{\hbar\omega_\gamma\sqrt{n}}{E_{c,n}^{(0)} - E_{v,n-1}^{(0)}}, \quad a_{n+1}' = \frac{\hbar\omega_\gamma\sqrt{n+1}}{E_{c,n}^{(0)} - E_{v,n+1}^{(0)}}, \\ b_{n-1}' &= \frac{\hbar\omega_\gamma\sqrt{n}}{E_{v,n}^{(0)} - E_{c,n-1}^{(0)}}, \quad b_{n+1}' = \frac{\hbar\omega_\gamma\sqrt{n+1}}{E_{v,n}^{(0)} - E_{c,n+1}^{(0)}}, \end{aligned}$$

and $a_{n\pm1} = a_{n\pm1}'/a_n$, $b_{n\pm1} = b_{n\pm1}'/b_n$. Note that we have neglected the correction to the wave function induced by H'' since it is too small.

III. MATRIX ELEMENTS FOR MAGNETO-OPTICAL TRANSITIONS

Within the linear-response theory, the dynamical conductivity can be written in the usual manner as [21–23]

$$\sigma_{\mu\nu}(\omega) = \frac{i\hbar e^2}{S_0}\sum_{\xi\neq\xi'}\frac{[f(E_\xi) - f(E_{\xi'})]\langle\xi|v_\mu|\xi'\rangle\langle\xi'|v_\nu|\xi\rangle}{(E_\xi - E_{\xi'})(E_\xi - E_{\xi'} + \hbar\omega + i\Gamma_\xi)}, \tag{11}$$

where ω is the photon frequency, $S_0 = L_xL_y$ is the sample area with the size L_x (L_y) in the $x(y)$ direction, $|\zeta\rangle = |s,n,k_x\rangle$ is the total wave function of the system where $s = +/-$ for the conduction/valence band, and $f(E_\xi) = [e^{(E_\zeta - E_F)/k_BT} + 1]^{-1}$ is the Fermi-Dirac distribution function with Boltzman constant k_B and temperature T. The sum runs over all states $|\xi\rangle = |s,n,k_x\rangle$ and $|\xi'\rangle = |s',n',k_x'\rangle$ with $\xi \neq \xi'$. In the simplest approximation, we include the disorder effect by replacing Γ_ξ with the phenomenological constant Γ and taking the ideal eigenstates as $|\xi\rangle$ and $|\xi'\rangle$. The velocity matrices $v_{x/y} = \partial H/\partial p_{x/y}$ are

$$\begin{aligned} v_x &= \begin{pmatrix} -v_1(\hat{a} + \hat{a}^\dagger) & v_f \\ v_f & r_x'v_1(\hat{a} + \hat{a}^\dagger) \end{pmatrix}, \\ v_y &= \begin{pmatrix} -iv_2(\hat{a} - \hat{a}^\dagger) & 0 \\ 0 & iv_2r_y'(\hat{a} - \hat{a}^\dagger) \end{pmatrix}, \end{aligned} \tag{12}$$

where $v_1 = \sqrt{\hbar\omega_c/2m_{cx}}$, $v_2 = \sqrt{\hbar\omega_c/2m_{cy}}$, $r_x' = 2r_x$, and $r_y' = 2r_y$. To calculate the matrix elements in Eq. (11), we cannot use the single-electron states in Eqs. (6) or (9) and (10) directly since they are only the envelope wave functions. The band-edge wave functions (BEWs) around the Γ point ($|\psi_{c/v}(\Gamma)\rangle$) will also play an important role in determination of the optical properties of BP TFs. The total wave function $|\xi\rangle$ is the direct product of the envelope functions and the BEWs. The BEWs of monolayer BP in the GW approximation are given by [24]

$$\begin{aligned} |\psi_c(\Gamma)\rangle &= 0.57|s\rangle + 0.44|p_x\rangle + 0.69|p_z\rangle, \\ |\psi_v(\Gamma)\rangle &= 0.17|s\rangle + 0.40|p_x\rangle + 0.90|p_z\rangle, \end{aligned} \tag{13}$$

where $|s\rangle$, $|p_x\rangle$, and $|p_y\rangle$ are the atomic orbits. The BEWs of BP TFs are currently unknown. In comparison with Eq. (13), they have the same ingredients but slightly different weights of atomic orbits. We thus take Eq. (13) as the BEWs of BP TFs. This approximation would not change the physics reported here. By means of the wave functions in Eqs. (6) and (13), the transition matrix elements of the velocity matrices for the same sub-band are calculated as

$$\begin{aligned} X_{n',n}^{s',s} &= \langle s',n',k_x'|v_x|s,n,k_x\rangle \\ &= \sum_{m',m}^{M}\big[v_f p\big(c_{m'}^{n',s'*}d_m^{n,s} + d_{m'}^{n',s'*}c_m^{n,s}\big)\delta_{m',m} \\ &\quad - v_1\sqrt{m}\big(c_{m'}^{n',s'*}c_m^{n,s} - r_x'd_{m'}^{n',s'*}d_m^{n,s}\big)\delta_{m',m-1} \\ &\quad - v_1\sqrt{m+1}\big(c_{m'}^{n',s'*}c_m^{n,s} - r_x'd_{m'}^{n',s'*}d_m^{n,s}\big)\delta_{m',m+1}\big], \end{aligned} \tag{14}$$

$$\begin{aligned} Y_{n,n'}^{s,s'} &= \langle s,n,k_x|v_y|s',n',k_x'\rangle \\ &= \sum_{m,m'}^{M} iv_2\big[\sqrt{m}\big(-c_m^{n,s*}c_{m'}^{n',s'} + r_y'd_m^{n,s*}d_{m'}^{n',s'}\big)\delta_{m',m-1} \\ &\quad + \sqrt{m+1}\big(c_m^{n,s*}c_{m'}^{n',s'} - r_y'd_m^{n,s*}d_{m'}^{n',s'}\big)\delta_{m',m+1}\big], \end{aligned} \tag{15}$$

where $p = \langle\psi_c(\Gamma)|\psi_v(\Gamma)\rangle = 0.839$. Note, we have omitted a delta function $\delta_{k_x,k_x'}$ in the derivation. The matrix elements between different sub-bands are zero since $|\varphi_j(z)\rangle$ and $|\varphi_{j'}(z)\rangle$ are orthogonal for $j \neq j'$. The total transition probability is

the sum of all the sub-bands below the photon energy. With those matrix elements, one can evaluate the longitudinal and Hall magneto-optical conductivity for linearly polarized light directly. Substituting Eqs. (14) and (15) into Eq. (11) and making the replacement $\sum_{k_x} \to g_s S_0/2\pi l_B^2$, where $g_s = 2$ for the spin degeneracy, we obtain the absorption (real) part of the longitudinal magneto-optical conductivity (LMOC) as

$$\frac{\mathrm{Re}\,\sigma_{\mu\mu}}{\sigma_0} = \sum_{n,n',s,s'} \frac{[f(E_{n',s'}) - f(E_{n,s})]\left|\mu_{n',n}^{s',s}\right|^2 \Gamma}{(E_{n,s} - E_{n',s'})[(E_{n,s} - E_{n',s'} + \hbar\omega)^2 + \Gamma^2]}, \tag{16}$$

where $\mu = (x, y)$, $x_{n',n}^{s',s} = \hbar X_{n',n}^{s',s}/l_B$, $y_{n',n}^{s',s} = \hbar Y_{n',n}^{s',s}/l_B$, and $\sigma_0 = 2e^2/h$. Similarly, the expression for the absorption (imaginary) part of the Hall magneto-optical conductivity is

$$\frac{\mathrm{Im}\,\sigma_{xy}}{\sigma_0} = \mathrm{Im} \sum_{n,n',s,s'} \frac{[f(E_{n',s'}) - f(E_{n,s})] x_{n',n}^{s',s} y_{n,n'}^{s,s'}}{(E_{n,s} -, E_{n',s'})(E_{n,s} - E_{n',s'} + \hbar\omega + i\Gamma)}. \tag{17}$$

On the other hand, in order to understand the numerical results better, one can obtain the matrix element for the interband transition analytically with the help of the eigenvectors in Eqs. (9), (10), and (13), which are given by

$$\langle \psi_{c,m} | v_{x/y} | \psi_{v,n} \rangle = A_{x/y}^{cm,vn} \delta_{m,n} + B_{x/y}^{cm,vn} \delta_{m,n-2} + C_{x/y}^{cm,vn} \delta_{m,n+2}, \tag{18}$$

where $M_{x/y}^{cm,vn}$ $(M = A, B, C)$ are presented by Eqs. (A4)–(A9) of Appendix A. From Eq. (18), we find that the interband transitions occur when the LL index changes $\Delta n = 0, \pm 2$, which is completely different from that of dipole type transitions reported in graphene [20,21], silicene [22], and the topological insulator [23,25]. This transition feature is also valid in monolayer BP according to our numerical calculations since the Hamiltonians are similar to each other. This difference comes from different calculations about the optical transition matrix. The previous studies [18] used the decoupled Hamiltonian [12] to calculate the transition matrices, where the interband coupling is omitted. Note that other kinds of transitions, such as $\Delta n = \pm 1, \pm 3, \pm 4, \ldots$, may occur when we include the correction to the wave functions in Eqs. (9) and (10) induced by H' and H'' to higher order, but they are too weak. Our results are different from that obtained by using the decoupled Hamiltonian [18], which neglected the influence of the interband coupling. Similarly, for intraband transitions of p-type BP TFs, the matrix elements are

$$\langle \psi_{v,m} | v_{x/y} | \psi_{v,n} \rangle = D_{x/y}^{vm,vn} \delta_{m,n-3} + E_{x/y}^{vm,vn} \delta_{m,n+3} + F_{x/y}^{vm,vn} \delta_{m,n-1} + G_{x/y}^{vm,vn} \delta_{m,n+1}, \tag{19}$$

where $M_{x/y}^{vm,vn}$ $(M = D, E, F, G)$ are presented in Eqs. (A11)–(A18) of Appendix A. From Eq. (19), we find that the intraband transition occurs when the LL index changes $\Delta n = \pm 1, \pm 3$. The intraband transition matrix elements of n-type BP thin films are similar to that of p-type ones.

IV. RESULTS AND DISCUSSIONS

A. Interband magneto-optical spectrum

In this section, we present the numerical results for the LL spectra and magneto-optical conductivities and discuss them using the analytical formulas. Hereafter, unless explicitly specified, the conductivities are all in units of $\sigma_0 = 2e^2/h$, temperature $T = 5$ K, and Fermi energy $E_F = 0$ for interband transitions.

Figures 2(a) and 2(b) present the LLs as a function of the magnetic field for the lowest sub-bands. As shown in the figure, the perturbed LLs (the blue dashed lines) are in good agreement with the numerical results (the red solid lines) in a wide regime of the magnetic field. This indicates that the perturbation method is reliable. Further, the Landau splittings of conduction and valence band are different for a fixed magnetic field [see Eq. (8)] due to the anisotropic effective masses at zero field. The interband coupling becomes more important with the increasing of LL index or magnetic field (see the green dash-dotted lines). As shown in Fig. 2(c), the LL spacings decrease with the increasing of the LL index. The stronger the magnetic field, the faster the LL spacing decreases, which can also be inferred from Eq. (8). This means that the LLs sublinearly depend on the LL index. Those decreasing LL spacings will induce a redshifting in the intraband magneto-optical conductivities. From Fig. 2(d), we find that the derivative of LLs $dE_{v,n}/dB$ in the valence band becomes dependent on the magnetic field with the increasing of the LL index, which again means that the LLs sublinearly

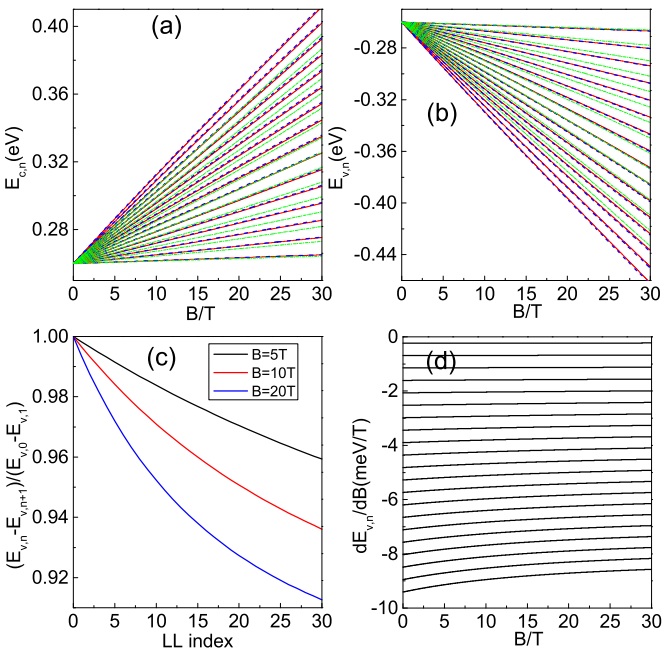

FIG. 2. (Color online) LLs as a function of the magnetic field for the lowest sub-bands. (a) and (b) represent for conduction and valence band, respectively. The red solid (blue dashed) lines represent the result obtained from numerical (perturbed) calculation. The green dash-dotted lines are eigenvalues of H_0 given in Eq. (5). The number of basis function used in the calculation is 200 to get convergent numerical results. (c) LL spacings of valence band (in unit of $E_{0,v} - E_{v,1}$) as a function of LL index. (d) Derivative of LL ($dE_{v,n}/dB$) in valence band as a function of magnetic field.

depend on the magnetic field. Similar conclusions can be drawn for the LLs in the conduction band.

Next, we consider the possibly allowed transitions for the interband process which are schematically illustrated in Fig. 1(d). Unusually, we find the interband transitions mainly occur when the LL index changes $\Delta n = 0, \pm 2$ according to Eq. (18), which is completely different from that of the dipole-type transition ($\Delta n = \pm 1$) reported in graphene [20,21], silicene [22], and the topological insulator [23,25]. Quantitatively, the velocities for the lowest regime of the sub-band are $v_f = 3.5 \times 10^5$ m/s, $v_1 = 1.3\sqrt{B} \times 10^4$ m/s, and $v_2 = 4.89\sqrt{B} \times 10^3$ m/s, which means that, in the moderate magnetic field regime $\approx B = 10$ T, v_f is one order (two orders) of magnitude larger than $v_1(v_2)$. Keeping this in mind and incorporating with the analytical results in Eq. (18), we obtain some basic features of the interband magneto-optical conductivities.

(i) Since the transition probability is proportional to the square of the velocities, we can expect that the LMOC for linearly polarized light along the armchair (x) direction is about *three* orders of magnitude larger than that along the zigzag (y) direction, which is consistent with the results obtained from tight-binding calculations in monolayer BP [17].

(ii) According to Eqs. (A4)–(A6), the LMOC along the x direction is dominated by the transitions $\Delta n = 0$ since the matrix element in Eq. (A4) is about one order larger than that in Eqs. (A5) and (A6). This dominated contribution decreases with the increasing magnetic field. According to Eqs. (A7)–(A9), the LMOC for linearly polarized light along the y direction is dominated by the transitions $\Delta n = \pm 2$ due to the absence of interband coupling.

(iii) Owing to the relatively small transition probability along the y direction, the interband Hall magneto-optical conductivity (HMOC) is closer to the LMOC along the y direction in magnitude than that along the x direction.

Figure 3 presents the real part of the LMOC and imaginary part of the HMOC as a function of photon energy under magnetic field $B = 10$ T and level broadening factor $\Gamma =$ 0.15 meV for interband transitions. Determined by the band gap (0.52 eV), the interband magneto-optical absorbtion of BP TFs occurs at the near infrared region. As shown in Fig. 3(a), $\mathrm{Re}\sigma_{xx}(\omega)$ is *three* orders of magnitude larger than $\mathrm{Re}\sigma_{yy}(\omega)$ due to the anisotropic band structure at zero field, which is in line with the results reported in monolayer BP utilizing tight-binding calculations [17]. In the high photon energy regime, we observe well-resolved three-peak structures corresponding to the transitions $\Delta n = 0, \pm 2$. As expected, owing to the interband coupling, $\mathrm{Re}\sigma_{xx}(\omega)$ is dominated by the transitions $\Delta n = 0$ and decreases with increasing photon energy since high index LLs are involved in the transition process in the high photon energy regime, which can also be inferred from Eq. (A4). In contrast, $\mathrm{Re}\sigma_{yy}(\omega)$ is dominated by the transitions $\Delta n = \pm 2$ due to the absence of interband coupling. We observe well-resolved two-peak structures in $\mathrm{Re}\sigma_{yy}(\omega)$ in the low photon energy regime. Further, the transitions of $\Delta n = 0$ become important with the increasing of the photon energy, which can be inferred from Eq. (A7). There are also some extra side peaks in $\mathrm{Re}\sigma_{yy}(\omega)$ arising from the correction to the wave functions in Eq. (10) induced by H'', but these are relatively small compared with the transitions of $\Delta n = 0, \pm 2$. In Fig. 3(b), we find that $\mathrm{Im}\sigma_{xy}(\omega)$ is closer to $\mathrm{Re}\sigma_{yy}(\omega)$ but two orders of magnitude less than $\mathrm{Re}\sigma_{xx}(\omega)$. This fact results from the large difference between the transition probability along the x direction and that along the y direction [see Eqs. (18) and (19)]. Again, in the high photon energy regime, we find well-resolved three (one positive and two negative) peaks in $\mathrm{Im}\sigma_{xy}(\omega)$, which indicates that the interband transitions mainly occur when the LL index changes $\Delta n = 0, \pm 2$. There exists a single positive peak in $\mathrm{Im}\sigma_{xy}$ since it only involves the transition between $E_{v,0}$ and $E_{c,0}$.

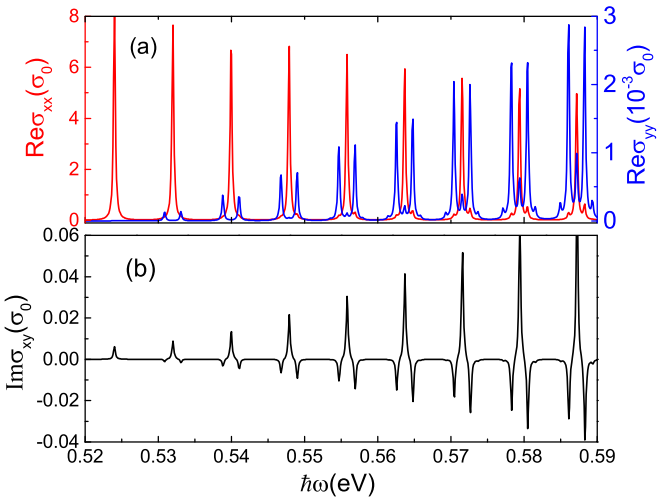

FIG. 3. (Color online) (a) The real part of the longitudinal magneto-optical conductivity and (b) imaginary part of the Hall magneto-optical conductivity (in units of $\sigma_0 = 2e^2/h$) as a function of the photon energy under the magnetic field $B = 10$ T and level broadening factor $\Gamma = 0.15$ meV.

Owing to the unusual interband optical transitions, i.e., $\Delta n = 0, \pm 2$, we may expect beating pattern oscillations in dynamical conductivities of the interband transition process for relatively large level broadening factor Γ. Figures 4 and 5 present the LMOC and Fig. 6 depicts the HMOC as a function of magnetic field for linearly polarized light. We take the photon energy $\hbar\omega = 0.8$ eV and Landau-level broadening factor $\Gamma = 0.5$ meV. According to Hamiltonian (2), the band gaps for the lowest four sub-bands in successive order are 0.52, 0.58, 0.67, 0.80 eV. Hence, the lowest three sub-bands will be excited for photon energy $\hbar\omega = 0.8$ eV. As shown in the figure, in the high magnetic field regime $B > 5$ T, we find well-resolved peak structures in $\mathrm{Re}\sigma_{\mu\mu}$ ($\mu = x, y$) and $\mathrm{Im}\sigma_{xy}$, which is similar to the peaks plotted in Fig. 3. At low magnetic field, a beating pattern oscillation appears in the magneto-optical conductivity due to the relatively large LL broadening factor Γ which induces the overlap of the nearest peaks contributed by three kinds of optical transitions $\Delta n = 0, \pm 2$. Those beating patterns will be quenched and convergent to the results in Fig. 3 in strong magnetic field or with tiny level broadening factors. However, the level broadening may be always relatively large since defects and impurities are unavoidable in realistic experimental samples and the pristine ones are difficult to obtain.

B. Intraband magneto-optical spectrum

Next, we turn to discuss the intraband transitions. The real parts of LMOCs for filling factor $\nu = 1$ to 3 (hole doped)

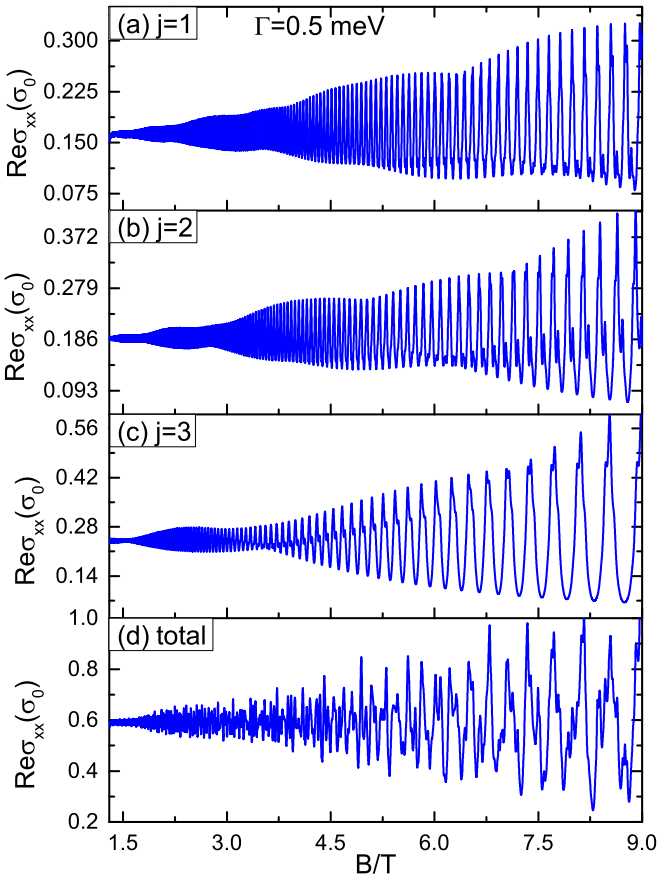

FIG. 4. (Color online) The real part of longitudinal magneto-optical conductivity for linearly polarized light along the x direction as a function of magnetic field under photon energy $\hbar\omega = 0.8$ eV and Landau-level broadening factor $\Gamma = 0.5$ meV. (a)–(c) represent the results for the lowest three sub-bands and (d) donates the total magneto-optical conductivity.

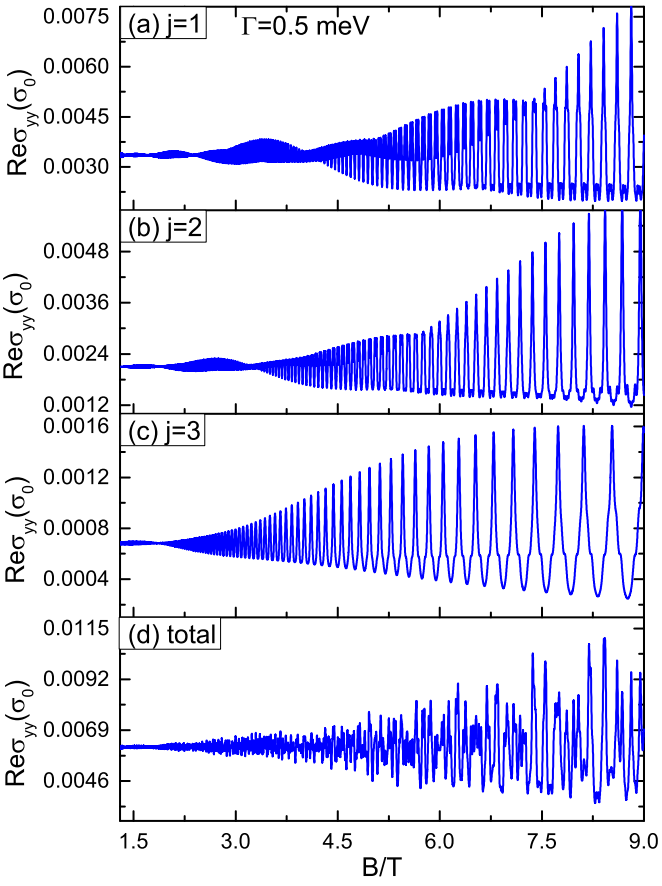

FIG. 5. (Color online) The real part of longitudinal magneto-optical conductivity for linearly polarized light along the y direction as a function of magnetic field under photon energy $\hbar\omega = 0.8$ eV and Landau-level broadening factor $\Gamma = 0.5$ meV. (a)–(c) represent the results for the lowest three sub-bands and (d) donates the total magneto-optical conductivity.

are shown in Figs. 7(a) and 7(b) for $|n+1\rangle \to |n\rangle$ and $|n+3\rangle \to |n\rangle$ transitions, respectively. The insets depict the transitions between the nearest LLs for cases with $\nu = 1$ to 3. We observe two groups of resonance peaks. One group corresponds to a particular transition process $|n+1\rangle$ to $|n\rangle$ and another corresponds to $|n+3\rangle$ to $|n\rangle$, which means that the intraband transitions mainly occur when the LL index changes $\Delta n = \pm 1, \pm 3$ according to Eq. (19). Both of them occur at the terahertz (THz) frequencies. We find that the dipole type transition is dominant in the intraband transition process, which can also be inferred from Eqs. (A11)–(A18). For the dipole-type transitions ($\Delta n = \pm 1$), $\mathrm{Re}\sigma_{xx}(\omega)$ is about seven times larger than $\mathrm{Re}\sigma_{yy}(\omega)$ [see Fig. 7(a)], which is just the ratio between the effective masses m_{vy} and m'_{vx}. Similarly, for the transitions $|n+3\rangle$ to $|n\rangle$, $\mathrm{Re}\sigma_{xx}(\omega)$ is exactly m_{vy}/m_{vx} times larger than $\mathrm{Re}\sigma_{yy}(\omega)$ according to Eqs. (A12) and (A16). In other words, those conductivity peaks can be used to determine the effective masses of hole bands at zero field. Contrary to the conventional case, we find that the resonant frequency is slightly redshifted with increasing doping, which is a reflection of the decreasing LL spacings [see Fig. 7(b)]. This redshift also increases with magnetic field as depicted in Fig. 2(c). We note that the frequency shift increases in almost uniform steps each time when the filling factor (LL index) decreases by 1. Interestingly, this redshifting behavior can be understood from Eq. (8) rather straightforwardly. This expression accounts for linear dependence of the resonance frequency on n quantitatively, and is a direct result of the interband coupling γ [see Eq. (8)]. In other words, this redshift in intraband LMOCs can be used to determine interband coupling γ in BP TFs. Similar conclusions can be drawn for the LMOC and LLs in the conduction band. Further, it is also worthy to mention that the LMOC calculated here can be directly measured through the magneto-optical transport experiment or magnetoabsorption and Faraday rotation experiments [19].

Further, we consider the effect of finite hole doping on the magneto-optical response of the 10-nm BP TFs including the effect of self-consistent potential with hole density 3.0×10^{12} cm^{-2}. The probability distribution and band profile for the lowest sub-band are shown in Fig. 1(c) and the detailed calculations are presented in Appendix B. From the figure, we find the band profile is nearly horizontal, which means that the band gap is almost unchanged. But the probability distribution is changed, which leads to a new overlap factor (0.968) for the envelope wave function of conduction and valence band along the z direction. This indicates that the magneto-optical

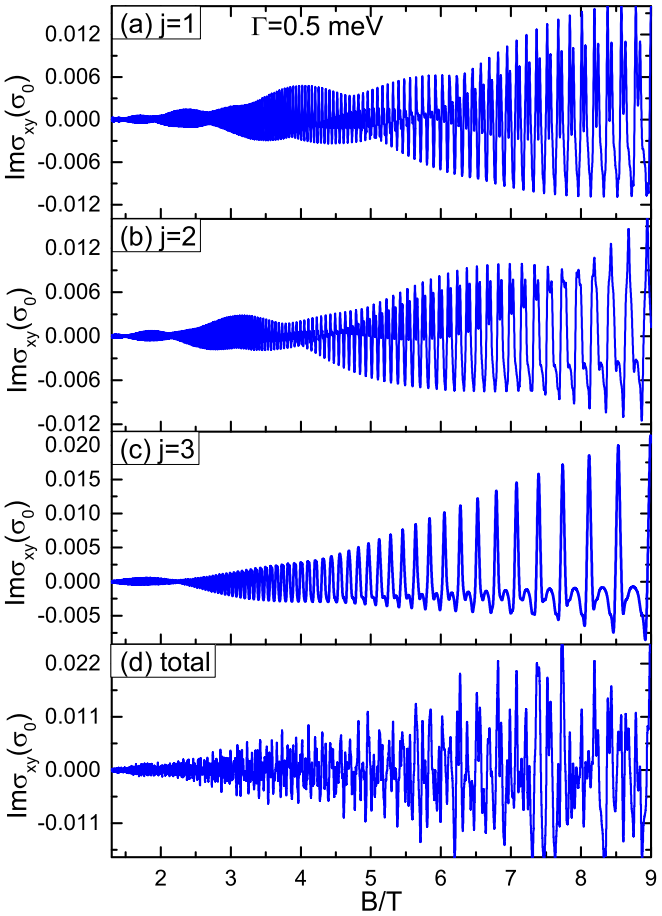

FIG. 6. (Color online) The imaginary part of Hall magneto-optical conductivity for linearly polarized light as a function of magnetic field under photon energy $\hbar\omega = 0.8$ eV and Landau-level broadening factor $\Gamma = 0.5$ meV. (a)–(c) represent the results for the lowest three sub-bands and (d) donates the total magneto-optical conductivity.

conductivity will be weakened by the self-consistent potential. However, the main features of the magneto-optical spectra reported here are unaffected since the confinement is only along the z direction. For a typical hole density 3.0×10^{12} cm^{-2}, the magneto-optical conductivity peaks in Fig. 3 involved with the lowest six LLs will disappear since the lowest six LLs

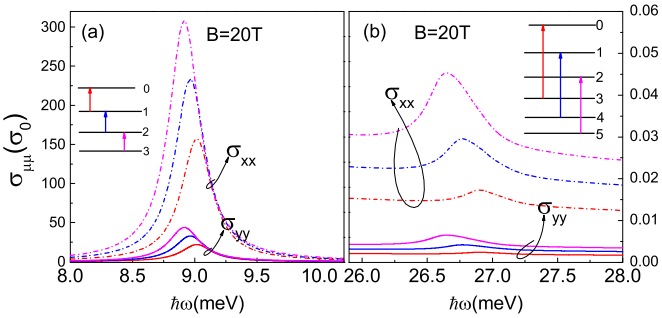

FIG. 7. (Color online) The real part of the longitudinal optical conductivity for intraband transition as a function of photon energy under magnetic field $B = 20$ T and level broadening factor $\Gamma = 0.1$ meV, for (a) $|n+1\rangle \rightarrow |n\rangle$ and (b) $|n+3\rangle \rightarrow |n\rangle$ transitions, respectively.

in the valence band are Pauli blocked [18,23]. The results presented in Figs. 4–6 remain unchanged since the photon energy (0.8 eV) used in our calculation is relatively large, which only excites the higher LLs in the valence band.

Finally, we should point out that our results about the MOC can also be applied to the monolayer BP. The unusual selection rules are determined by the interband coupling γ. It always exists when the layer number reduces. According to the magneto-optical transition matrix elements in Appendix A, the highly anisotropic MOC mainly arises from the large ratio between v_f and v_2. This ratio remains unchanged with the decreasing of the thickness of BP TFs. Moreover, the optical transition energies will be shifted if one includes the excitonic effect, which is similar to that in graphene [26].

V. SUMMARY

We theoretically investigated the Landau levels and magneto-optical conductivity of black phosphorus thin films under a perpendicular magnetic field based on an effective $\boldsymbol{k}\cdot\boldsymbol{p}$ Hamiltonian and linear-response theory. We obtained the analytical expression for LLs, which agrees well with the numerical calculations, and find that the LLs sublinearly depend on the magnetic field and LL index. By using the Kubo formula, we evaluated the longitudinal and Hall optical conductivities as functions of the photon energy and the magnetic field. The analytical optical transition matrix elements reveal unusual selection rules for the interband (intraband) optical transitions between the LLs $\Delta n = 0, \pm 2$ ($\pm 1, \pm 3$). The MOC spectra show strongly anisotropic behaviors of the band structure. For the interband transition, the MOC for linearly polarized light along the armchair direction is three orders of magnitude larger than that along the zigzag direction. Interestingly, we found a beating pattern in the interband MOC due to the interference among the three kinds of optical transitions. For the intraband transition, the MOC can be used to determine the band parameters such as the effective masses and the interband coupling at zero magnetic field. Our results about the MOC can also be applied to monolayer black phosphorus.

ACKNOWLEDGMENTS

This work was supported by Grant No. 2011CB922204 from the MOST of China and the National Natural Science Foundation (Grants No. 11434010, No. 11174252, No. 11304306, and No. 61290303).

APPENDIX A

According to Eqs. (8), (9), and (13), we obtain the total wave function for conduction and valence band as

$$|\psi_{c,n}\rangle = \begin{pmatrix} a_n|n\rangle|\psi_c(\Gamma)\rangle \\ (a_{n-1}|n-1\rangle + a_{n+1}|n+1\rangle)|\psi_v(\Gamma)\rangle \end{pmatrix}, \quad \text{(A1)}$$

$$|\psi_{v,n}\rangle = \begin{pmatrix} (b_{n-1}|n-1\rangle + b_{n+1}|n+1\rangle)|\psi_c(\Gamma)\rangle \\ b_n|n\rangle|\psi_v\Gamma)\rangle \end{pmatrix}. \quad \text{(A2)}$$

Taking Eqs. (A1) and (A2) and incorporating with the velocity matrix in Eq. (12), we obtain the matrix elements

for the interband transition as

$$\langle\psi_{c,m}|v_{x/y}|\psi_{v,n}\rangle = A_{x/y}^{cm,vn}\delta_{m,n} + B_{x/y}^{cm,vn}\delta_{m,n-2} + C_{x/y}^{cm,vn}\delta_{m,n+2}, \tag{A3}$$

with

$$A_x^{cm,vn} = v_f p(a_{m-1}b_{n-1} + a_m b_n + a_{m+1}b_{n+1}) - v_1[a_m(b_{n+1}\sqrt{n+1} + b_{n-1}\sqrt{n}) - r_x' b_n(a_{m-1}\sqrt{n} + a_{m+1}\sqrt{n+1})], \tag{A4}$$

$$B_x^{cm,vn} = v_f p a_{m+1}b_{n-1} - v_1(a_m b_{n-1}\sqrt{n-1} - r_x' a_{m+1}b_n\sqrt{n}), \tag{A5}$$

$$C_x^{cm,vn} = v_f p a_{m-1}b_{n+1} - v_1(a_m b_{n+1}\sqrt{n+2} - r_x' a_{m-1}b_n\sqrt{n+1}), \tag{A6}$$

$$A_y^{cm,vn} = -i v_2[a_m(b_{n+1}\sqrt{n+1} - b_{n-1}\sqrt{n}) - r_y' b_n(a_{m-1}\sqrt{n} - a_{m+1}\sqrt{n+1})], \tag{A7}$$

$$B_y^{cm,vn} = -i v_2(a_m b_{n-1}\sqrt{n-1} - r_y' a_{m+1}b_n\sqrt{n}), \tag{A8}$$

$$C_y^{cm,vn} = i v_2(a_m b_{n+1}\sqrt{n+2} - r_y' a_{m-1}b_n\sqrt{n+1}), \tag{A9}$$

while, for the intraband transition process of p-type BP TFs, the matrix elements are

$$\langle\psi_{v,m}|v_{x/y}|\psi_{v,n}\rangle = D_{x/y}^{vm,vn}\delta_{m,n-3} + E_{x/y}^{vm,vn}\delta_{m,n+3} + F_{x/y}^{vm,vn}\delta_{m,n-1} + G_{x/y}^{vm,vn}\delta_{m,n+1}, \tag{A10}$$

with

$$D_x^{vm,vn} = -v_1 b_{m+1}b_{n-1}\sqrt{n-1}, \tag{A11}$$

$$E_x^{vm,vn} = -v_1 b_{m-1}b_{n+1}\sqrt{n+2}, \tag{A12}$$

$$F_x^{vm,vn} = v_f p(b_m b_{n-1} + b_{m+1}b_n) - v_1(b_{m-1}b_{n-1}\sqrt{n-1} + b_{m+1}b_{n+1}\sqrt{n+1} + b_{m+1}b_{n-1}\sqrt{n} - r_x' b_m b_n\sqrt{n}), \tag{A13}$$

$$G_x^{vm,vn} = v_f p(b_m b_{n+1} + b_{m-1}b_n) - v_1(b_{m-1}b_{n+1}\sqrt{n+1} + b_{m-1}b_{n-1}\sqrt{n} + b_{m+1}b_{n+1}\sqrt{n+2} - r_x' b_m b_n\sqrt{n+1}), \tag{A14}$$

$$D_y^{vm,vn} = -i v_2 b_{m+1}b_{n-1}\sqrt{n-1}, \tag{A15}$$

$$E_y^{vm,vn} = i v_2 b_{m-1}b_{n+1}\sqrt{n+2}, \tag{A16}$$

$$F_y^{vm,vn} = i v_2(b_{m+1}b_{n-1}\sqrt{n} - b_{m-1}b_{n-1}\sqrt{n-1} - b_{m+1}b_{n+1}\sqrt{n+1} + r_y' b_m b_n\sqrt{n}), \tag{A17}$$

$$G_y^{vm,vn} = i v_2(b_{m+1}b_{n+1}\sqrt{n+2} + b_{m-1}b_{n-1}\sqrt{n} - b_{m-1}b_{n+1}\sqrt{n+1} - r_y' b_m b_n\sqrt{n+1}). \tag{A18}$$

The matrix elements for the intraband transition process of n-type BP thin films are similar to those in p-type ones. With those matrix elements, we can evaluate the ac conductivity directly by using the Kubo formula.

APPENDIX B

In this Appendix, we calculate the electronic structure of the BP TFs including the influence of the self-consistent potential. We only need to consider the k_z dependent part in Hamiltonian (1) since the confinement is applied in the z direction. Therefore, the low-energy $\boldsymbol{k}\cdot\boldsymbol{p}$ is

$$H_z = \begin{pmatrix} \eta_c k_z^2 & 0 \\ 0 & -\eta_v k_z^2 \end{pmatrix} + V(z), \tag{B1}$$

where $V(z)$ describes the confining potential in the out-of-plane direction, including an internal electrostatic potential $V_{\text{in}}(z)$ caused by charge distribution in BP TFs. The total Hamiltonian then becomes $H = H_z + V_{\text{in}}(z)$. The sub-band dispersion and the corresponding eigenstates can obtained numerically from the Schrödinger equation

$$H\varphi_j = E\varphi_j, \tag{B2}$$

where j is the sub-band index, and φ_j is the envelope function.

To solve the Schrödinger equation, we adopt the hard wall boundary condition and use the finite difference method [27]. The internal electrostatic potential $V_{\text{in}}(z)$ is determined by the Poisson equation

$$\frac{d^2 V_{\text{in}}(z)}{dz^2} = -\frac{[n(z) + p(z)]}{\varepsilon}, \tag{B3}$$

where $n(z)$ and $p(z)$ are the densities of electrons and holes in the z direction, respectively, and ε is the dielectric constant. $n(z)$ and $p(z)$ can be obtained from [28,29]

$$n(z) = \sum_i n_i \left|\varphi_i^c(z)\right|^2, \quad p(z) = \sum_i p_i \left|\varphi_i^v(z)\right|^2, \tag{B4}$$

where c and v refer to the conduction band and valence band, respectively, and

$$\begin{aligned} n_i &= -m_i^{c*}|e|\frac{k_B T}{\pi\hbar^2}\ln\left(e^{\frac{E_f - E_i^c}{k_B T}} + 1\right), \\ p_i &= m_i^{v*}|e|\frac{k_B T}{\pi\hbar^2}\ln\left(e^{\frac{E_i^v - E_f}{k_B T}} + 1\right). \end{aligned} \tag{B5}$$

Here E_f is the Fermi energy, and m^* refers to the effective mass given by [28] $\sqrt{m_x^* m_y^*}$. We obtain the eigenstates and eigenvectors of the BP TFs numerically by solving the Schrödinger and Poisson equation self-consistently [28,29].

[1] T. Nishii, Y. Maruyama, T. Inabe, and I. Shirotani, Synth. Met. **18**, 559 (1987).

[2] A. S. Rodin, A. Carvalho, and A. H. Castro Neto, Phys. Rev. Lett. **112**, 176801 (2014).

[3] Likai Li, Yijun Yu, Guojun Ye, Qingqin Ge, Xuedong Ou, Hua Wu, Donglai Feng, Xian Hui Chen, and Yuanbo Zhang, Nat. Nanotechnol. **9**, 372 (2014).

[4] C. Q. Han, M. Y. Yao, X. X. Bai, Lin Miao, Fengfeng Zhu, D. D. Guan, Shun Wang, C. L. Gao, Canhua Liu, Dong Qian, Y. Liu, and Jin-feng Jia, Phys. Rev. B **90**, 085101 (2014).

[5] Han Liu, Adam T. Neal, Zhen Zhu, Zhe Luo, Xianfan Xu, David Tománek, and Peide D. Ye, Acs Nano. **8**, 4033 (2014).

[6] Andres Castellanos-Gomez, Leonardo Vicarelli, Elsa Prada, Joshua O. Island, K. L. Narasimha-Acharya, Sofya I. Blanter, Dirk J. Groenendijk, Michele Buscema, Gary A. Steele, J. V. Alvarez, Henny W. Zandbergen, J. J. Palacios, and Herre S. J. van der Zant, 2D Mater. **1**, 025001 (2014).

[7] Wanglin Lu, Haiyan Nan, Jinhua Hong, Yuming Chen, Chen Zhu, Zheng Liang, Xiangyang Ma, Zhenhua Ni, Chuanhong Jin, and Ze Zhang, Nano. Res. **7**, 853 (2014).

[8] Michele Buscema, Dirk J. Groenendijk, Sofya I. Blanter, Gary A. Steele, Herre S. J. van der Zant, and Andres Castellanos-Gomez, Nano. Lett. **14**, 3347 (2014).

[9] Ruixiang Fei, Vy Tran, and Li Yang, Phys. Rev. B **91**, 195319 (2015).

[10] Tony Low, A. S. Rodin, A. Carvalho, Yongjin Jiang, Han Wang, Fengnian Xia, and A. H. Castro Neto, Phys. Rev. B **90**, 075434 (2014).

[11] Vy Tran, Ryan Soklaski, Yufeng Liang, and Li Yang, Phys. Rev. B **89**, 235319 (2014).

[12] X. Y. Zhou, R. Zhang, J. P. Sun, Y. L. Zou, D. Zhang, W. K. Lou, F. Cheng, G. H. Zhou, F. Zhai, and Kai Chang, Sci. Rep. **5**, 12295 (2015).

[13] Likai Li, Guo Jun Ye, Vy Tran, Ruixiang Fei, Guorui Chen, Huichao Wang, Jian Wang, Kenji Watanabe, Takashi Taniguchi, Li Yang, Xian Hui Chen, and Yuanbo Zhang, Nat. Nanotech. **10**, 608 (2015).

[14] Xiaolong Chen, Yingying Wu, Zefei Wu, Shuigang Xu, Lin Wang, Yu Han, Weiguang Ye, Tianyi Han, Yuheng He, Yuan Cai, and Ning Wang, Nat. Commun. **6**, 7315 (2015).

[15] Likai Li, Fangyuan Yang, Guo Jun Ye, Zuocheng Zhang, Zengwei Zhu, Wen-Kai Lou, Liang Li, Kenji Watanabe, Takashi Taniguchi, Kai Chang, Yayu Wang, Xian Hui Chen, and Yuanbo Zhang, arXiv:1504.07155.

[16] Yongjin Jiang, Rafael Roldán, Francisco Guinea, and Tony Low, Phys. Rev. B **92**, 085408 (2015).

[17] Shengjun Yuan, A. N. Rudenko, and M. I. Katsnelson, Phys. Rev. B **91**, 115436 (2015).

[18] M. Tahir, P. Vasilopoulos, and F. M. Peeters, Phys. Rev. B **92**, 045420 (2015).

[19] I. Crassee, J. Levallois, A. L. Walter, M. Ostler, A. Bost-wick, E. Rotenberg, T. Seyller, D. Van Der Marel, and A. B. Kuzmenko, Nat. Phys. **7**, 48 (2011).

[20] V. P. Gusynin, S. G. Sharapov, and J. P. Carbotte, Phys. Rev. Lett. **98**, 157402 (2007).

[21] Mikito Koshino and Tsuneya Ando, Phys. Rev. B **77**, 115313 (2008).

[22] C. J. Tabert and E. J. Nicol, Phys. Rev. Lett. **110**, 197402 (2013).

[23] Zhou Li and J. P. Carbotte, Phys. Rev. B **88**, 045414 (2013).

[24] A. N. Rudenko and M. I. Katsnelson, Phys. Rev. B **89**, 201408(R) (2014).

[25] M. Orlita, B. A. Piot, G. Martinez, N. K. Sampath Kumar, C. Faugeras, M. Potemski, C. Michel, E. M. Hankiewicz, T. Brauner, Č. Drašar, S. Schreyeck, S. Grauer, K. Brunner, C. Gould, C. Brüne, and L. W. Molenkamp, Phys. Rev. Lett. **114**, 186401 (2015).

[26] L. A. Chizhova, J. Burgdörfer, and F. Libisch, Phys. Rev. B **92**, 125411 (2015).

[27] J. C. Light, I. P. Hamilton, and J. V. Lill, J. Chem. Phys. **82**, 1400 (1985).

[28] F. Stern, Phys. Rev. Lett. **18**, 546 (1967).

[29] F. Stern, Phys. Rev. B **5**, 4891 (1972).